Proceedings of the ASME 2010 International Mechanical Engineering Congress & Exposition
IMECE2010
November 12-18, 2010, Vancouver, British Columbia, Canada

IMECE2010-37324

TURBULENT BOUNDARY LAYER SEPARATION CONTROL BY USING DBD PLASMA ACTUATORS: PART Ⅰ－ EXPERIMENTAL INVESTIGATION

Xiaofei Xu
Ecole Polytechnique de Montreal
Montreal, QC, Canada

Huu Duc Vo
Ecole Polytechnique de Montreal
Montreal, QC, Canada

Njuki Mureithi
Ecole Polytechnique de Montreal
Montreal, QC, Canada

Xue Feng Zhang
National Research Council Canada
Ottawa, ON, Canada

ABSTRACT

Turbulent boundary layer separation is an important issue for a variety of applications, one of which is S-shaped aircraft engine intakes. The turbulent separation at the engine intake causes inlet flow distortion, which can deteriorate engine performance, cause fatigue and reduce engine component life. Various flow control techniques have been applied for turbulent boundary layer separation control, such as vortex generators, vortex generator jets and synthetic jets. The recent advent of dielectric barrier discharge (DBD) plasma actuators can potentially provide a robust method for the control of turbulent boundary layer separation. Compared to other flow control techniques, these new actuators are simple, robust and devoid of moving mechanical parts, which make them ideal for aerodynamic applications.

The present work studies the effects of DBD plasma actuators on the suppression of 2-D turbulent boundary layer separation induced by an imposed adverse pressure gradient. First, the flow field with and without actuation in a low-speed wind tunnel is investigated experimentally by Particle Image Velocimetry (PIV) measurements. The results show that plasma actuation can suppress turbulent boundary layer separation in both continuous and pulsed modes. In the pulsed mode, the actuation with an optimal actuation frequency, corresponding to a dimensionless frequency of order one, is found to most effectively suppress the turbulent separation. Moreover, the effects of plasma actuation on the flow is demonstrated and analyzed by using Proper Orthogonal Decomposition (POD). The effect of the actuation is found to be correlated to the second POD mode which corresponds to large flow fluctuations.

Keywords: turbulent boundary layer separation, plasma actuator, flow control, POD

1. INTRODUCTION

Inlet total-pressure distortion is common in engine intakes, especially in cross-wind conditions or for non-axial engine intakes. The reduced velocity in the distorted region of the engine face is detrimental to engine performance and causes undesirable fluctuating forces on the turbomachinery blades as they pass in and out of this region, which may lead to fatigue and shortened engine component life. Moreover, the inlet distortion reduces the stall margin of the fan and compressor and can result in engine surge, a flow instability characterized by flow oscillation across the engine, a catastrophic drop in thrust and damage to the engine.

Aircraft design considerations, such as in the case of turboprops and helicopters, can force the use of non-axial S-shaped engine inlets. The main cause of inlet distortion in this widely used intake geometry is the secondary flow and flow separation within the inlet duct itself, either from the curvature of inside wall bends or from high diffusion rates. The boundary layer separation in a realistic engine intake is usually turbulent, as a result of high Reynolds number and high adverse pressure gradient, resulting in boundary layer transition near the intake lip.

As shown in Fig. 1, for steady free-stream 2-D flows on streamlined surfaces, separation begins intermittently at a given location, i.e., the flow reversal occurs only over a fraction of the total time. The time fraction of forward flow decreases progressively downstream. For turbulent boundary layer separation with steady free-stream flow, Simpson [1] suggested

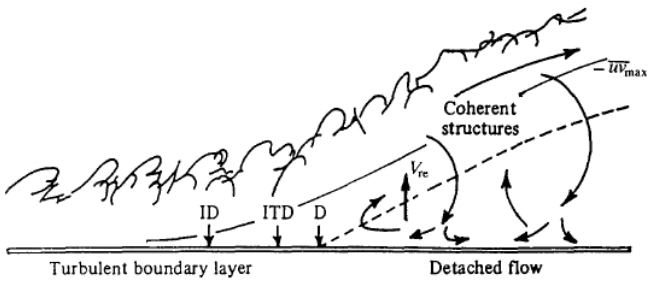

Figure 1: Turbulent boundary layer separation with turbulent structures supplying the small mean backflow (Simpson [2])

the following quantitative definitions on the flow detachment, with the definitions based on the forward-flow-fraction γ_{pu}. Incipient Detachment (ID) occurs with instantaneous backflow 1% of the time (γ_{pu} = 0.99); Intermittent Transitory Detachment (ITD) occurs with instantaneous backflow 20% of the time (γ_{pu} = 0.8); Transitory Detachment (TD) occurs with instantaneous backflow 50% of the time (γ_{pu} = 0.5); and Detachment (D) occurs with the time-averaged wall shear stress τ_w = 0. Simpson indicates that TD and D occur at the same axial location according to available data. In Fig. 1, the dashed line represents locations of zero mean axial velocity U; the solid line represents locations of maximum turbulent shear stress; and V_{re} represents the mean re-entrainment velocity along U= 0.

A large body of literature pertaining to boundary layer separation control and flow control in S-shaped inlet ducts exists. Sullerey et al. [3] studied the effect of various fences and vortex generator configurations in reducing distortion and improving total pressure recovery in 2-D diffusing S-ducts. Pradeep and Sullerey [4] later investigated the performance enhancement of 3-D diffusing S-ducts by secondary flow and separation control using vortex generator jets (VGJs). The VGJs (active flow control) were shown to be significantly more effective than tapered fin vortex generators (passive flow control). Moreover, an attempt was made to explain the physical mechanism of VGJs in secondary flow and separation control. The larger the size of the vortex, the more the mixing of the low-momentum boundary layer fluid with the high-momentum free-stream fluid and the more effective was the flow control. Separation control using zero-net-mass-flow (ZNMF) jets in diffusing S-ducts was studied by Mathis et al. [5]. The ZNMF jet actuators are unsteady flow control devices for which one of the important parameters is actuation frequency or Strouhal number (based on the rms velocity and the diameter of the ZNMF jet). With the ZNMF actuator located close to the time-averaged separation point operating at the most effective actuation frequency (corresponding to the most spatially unstable mode in the uncontrolled flow), only a very low energy input was necessary to suppress the separation in a duct with high degree of curvature.

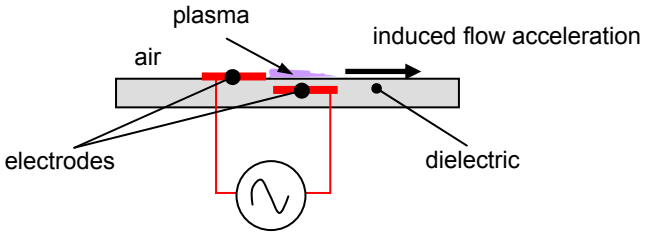

Figure 2: A schematic representation of plasma actuator

In spite of their effectiveness, there are some practical considerations that impede the use of the previously listed active flow control devices in real engine operating conditions. VGJs require an air supply system, likely taken from engine bleed, and associated pipes and valves, which imply penalty in engine performance and in weight. ZNMF jets require a system with oscillating mechanical parts that may limit the robustness of the actuator under operational conditions. Moreover, there is a risk of clogging of the orifices, especially if small actuators are used to minimize actuation power and response time. Compared to these relatively complex actuators, another active flow control technique, which is being more widely researched, is plasma-based actuation. Plasma-based actuation is generally based on the following mechanisms [6]: 1) thermal effect, i.e., rapid gas heating resulting from the Joule dissipation, such as direct-current (DC) filamentary discharges, 2) non-thermal effect, i.e., magneto-hydrodynamic (MHD) or electro-hydrodynamic (EHD) forcing by exerting forces to accelerate or decelerate the gas in the flow, such as DC glow discharges and single dielectric barrier discharge (DBD). The DBD plasma actuator is a fairly simple and robust device without moving parts that can effectively induce laminar-turbulent transition, and suppress and/or delay boundary layer separation. A typical DBD plasma actuator, as illustrated in Fig. 2, consists of two electrodes arranged asymmetrically, one exposed to the air and the other hidden beneath a layer of dielectric material. When the electrodes are subjected to a sufficiently high amplitude AC voltage (~1-10 kV_{pp}) at high frequency (~1-10 kHz), the air above the hidden electrode partially ionizes. In the presence of the electric field, this results in a flow acceleration (momentum addition to the flow) near the surface. More information on plasma actuators can be found in [7-9].

The DBD plasma actuator can be used in continuous mode or pulsed mode (steady or unsteady actuation). For the latter mode, the significant parameters, as shown in Fig. 3, include actuation frequency ($1/T_c$), duty cycle and strength. The continuous mode can be regarded as a duty cycle of 100%. In the pulsed mode, the pulsing frequency can be chosen to excite resonant turbulent flow structures in the boundary layer to improve momentum transfer from the outer high-velocity fluid and thus suppress separation with minimal power input.

Many researchers have studied the application of plasma actuators, e.g., lift increase on airfoils [10, 11], separation control on gas turbines [12] and vortex control on delta wings [13]. The research and results of plasma actuation, however,

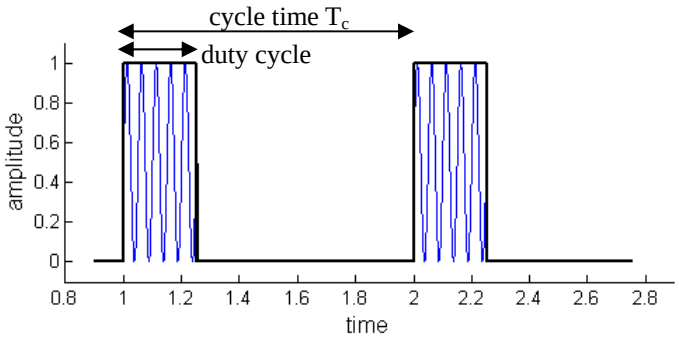

Figure 3: An illustration of pulsed actuation

mainly focus on the suppression of laminar separation [14, 15] and laminar-turbulent transition, which are very receptive to imposed small-amplitude disturbance [16]. Research on the control of the much tougher turbulent separation [17, 18] by plasma actuation is just beginning. In order to achieve sufficient control authority for turbulent boundary layers, the actuator amplitude must be above a certain threshold level.

The present work is part of a project to study the effects of DBD plasma actuators both experimentally and numerically on suppression of a 2-D turbulent boundary layer separation induced by an imposed adverse pressure gradient. In the present paper, the flow field with and without actuation in a low-speed wind tunnel is investigated by particle image velocimetry (PIV) measurements. The effects of plasma actuation on the flow is then demonstrated and analyzed by using Proper Orthogonal Decomposition (POD). Part II of this work aims to develop and validate a simulation tool that captures the effects of plasma actuators on the flow, and carry out a parametric study of the concept at flow regimes beyond the flow control capability of plasma actuators of conventional strength.

2. EXPERIMENTAL FACILITY AND DATA ANALYSIS

2.1 Experimental Setup

Plasma Actuator

The plasma actuator utilized in this experiment is illustrated in Fig. 4. The two electrodes made of tinned copper foil are separated by a Teflon sheet of 12.7 mm thickness and 150 mm width. The electrodes span only 130 mm, leaving 10 mm from either side-wall to avoid wall effects. The upper and lower electrodes have a width of 12.7 mm and 25.4 mm, respectively. The upper electrode is connected to a sinusoidal AC signal generated by a Minipuls6 generator from Electrofluidsystems, while the lower electrode is grounded and insulated from air by the Kapton film. The Minipuls6 generator is designed to generate high frequency and high voltages AC signal in a range from 5 to 30 kHz with amplitudes up to 68 kV_{pp} (peak-to-peak voltage). The device consists of one integrated low-voltage-control-circuit board and a high voltage transformer cascade. The power is supplied from a DC power supply (Voltcraft PS 3620). The whole plasma actuator is inserted into the grooved flat plate. The position of the actuator

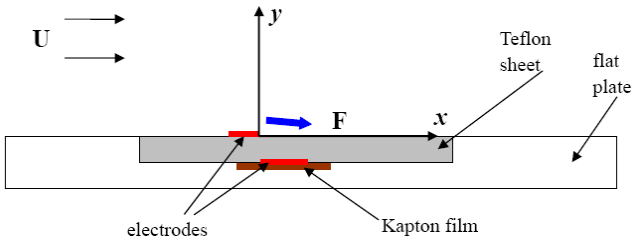

Figure 4: Configuration of plasma actuator implementation

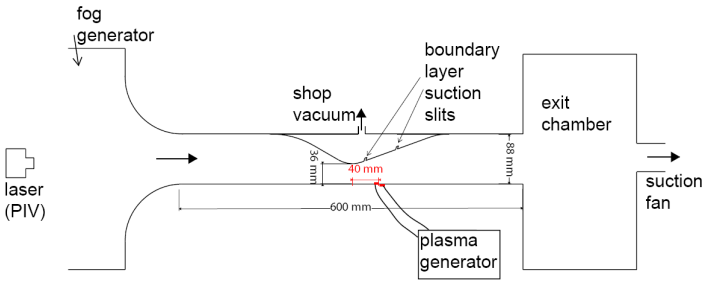

Figure 5: Configuration of experimental setup

(origin of the coordinates) is referred to the trailing edge of the upper (exposed) electrode. The effect of the plasma actuator can be represented by a body force (actuator strength).

In the present work, the plasma is generated at the voltage of 41.6 kV_{pp} and the frequency of 13.5 kHz, which corresponds to the predicted total body force (actuator strength) value around 40 mN/m. Both continuous and pulsed actuations are tested. For the pulsed mode, a 30% duty cycle (duty cycle for pulsed excitation is usually chosen smaller than 50% [13]) is chosen with different actuation frequencies of 5 Hz, 15 Hz and 25 Hz (discussed later).

Wind Tunnel and Test Section

A small-scale open-loop suction-type wind tunnel has been designed and constructed in the Wind Tunnel Laboratory of Ecole Polytechnique de Montreal. The wind tunnel, shown in Fig. 5, has a bell-mouth, a convergent-divergent test section and an exit chamber. The test section has a cross-section, at the diffuser exit, of 150 mm width and 88 mm height. The area ratio of throat to exit is 0.41. The main flow is generated by a suction fan connected to the exit chamber. The contoured upper wall imposes a desired pressure distribution on the bottom (lower) wall in the test section. To avoid the flow separation on the upper wall, suction slits are made on the diverging section of the upper wall, and are connected to a shop vacuum, to remove the upper wall boundary layer. Throat flow velocity (without actuation) for the experiment is 4.9 m/s. The plasma actuator is placed 40 mm downstream of the throat. A plexiglass window on the side-wall provides the optical access for PIV measurement.

2.2 Measurement Techniques

PIV Measurements

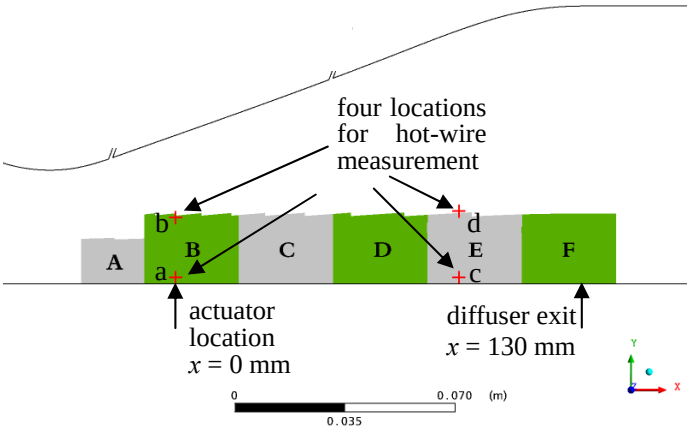

Figure 6: An illustration of windows for PIV measurement and four locations for hot-wire measurement

Particle Image Velocimetry (PIV) is used to investigate the flow characteristics in the diffuser. The Dantec Dynamics system consists of a Nd:YAG laser (New Wave, Solo PIV I-15, maximum repetition rate of 15 Hz) and a CCD camera (Flow Sense M2, 1600×1186 pixels). To seed the flow a particle generator (PIVTEC, Aerosol Generator PivPart30) is used. Upstream of the bellmouth, an inlet chamber is used to achieve a uniform concentration of seeding particles, which are suctioned into the test section for PIV measurement. The laser light sheet is directed into the test section (with the sheet plane at half the spanwise position) from the far upstream location. The images are captured by the camera at one side of the wind tunnel through the rectangular plexiglass windows. Fig. 6 shows the diffuser test section with the six PIV measurement windows highlighted. These windows cover the range from the diffuser throat to the exit plane. The windows B through F are 30 mm long by 21 mm high, while window A is 20 mm long by 14 mm high. The software Flow Manager is used for handling the measurements and for computing the velocity vector fields from the captured pictures. The velocity components are computed using a cross-correlation algorithm with adaptive multipass, interrogation windows of 32×32 pixels and an overlap of 50 %. The spatial resolution of the PIV measurement is 0.3 mm (16 pixels). The near-wall flow (y < 0.6 mm) cannot be captured because of wall reflection. In the present work, the sampling frequency is chosen as 14 Hz and thus each cycle of large fluctuations in the flow with pulsed actuation has 14 phase-fixed sampling points, assuming that the frequency of large fluctuations is locked on the actuation frequency (5 Hz, 15 Hz and 25 Hz). The duration dt between two successive image pairs ranges from 60 to 120 μs, depending on the imaging location with associated different velocity scales. 140 image pairs are acquired at each location.

Hot-Wire Measurements

A constant voltage hot-wire anemometer (CVA) is used to capture the resonant frequencies in the uncontrolled flow with turbulent boundary layer separation. The CVA is a type of hot-wire or hot-film anemometer specifically designed for high-bandwidth, high-sensitivity flow measurement. The hot-wire anemometer used in this work is a CVA-VC04 from Tao Systems, which has a frequency response bandwidth of around 400 kHz. The hot-wire probe is inserted into the test section from the upper wall, and is traversed in the vertical direction.

2.3 Proper Orthogonal Decomposition (POD) for Data Analysis

Proper orthogonal decomposition (POD) is a method to extract a reduced number of typical modes in a signal associated with their time evolution [19]. These signals can be pressure or velocity, obtained by experimental measurements or numerical simulations. The detailed equations and definitions can be found in the appendix. The POD offers representation of time-evolving vector field by using energetic spatial and temporal modes called *topos* and *chronos*, respectively. The energy contained in different modes decreases with increasing mode number (order), with the first mode normally corresponding to the mean field. Moreover, the entropy H, a normalized factor, can be used to compare the disorder levels of different signals. If all the energy is concentrated in the first mode, H is zero. In contrast, if the energy is uniformly distributed among all the modes, H attains its maximum value 1. Aubry et al. [20] suggested the entropy H as an effective way to detect the laminar-to-turbulent transition.

The POD has been used to extract the coherent structures in the separated shear layer around a wing by Hoarau et al. [21], and in the turbulent separation bubble by Mathis et al. [22]. In this paper, POD is also proposed to extract the coherent structures in the flow with turbulent boundary layer separation, and to quantify the effects of different plasma actuation regimes on boundary layer separation control.

3. RESULTS AND DISCUSSIONS

3.1 Mean Flow

Fig. 7 shows the velocity vectors and contours of the axial velocity from PIV measurements for the case without plasma actuation, while Fig. 8 shows the corresponding streamlines and contours of spanwise vorticity (normal to paper). It should be noted that both figures represent time-averaged flow fields. Without flow control, the laminar boundary layer on the flat plate separates just downstream of the throat, as seen in Fig. 7(a). The separated boundary layer then goes through laminar-turbulent transition and finally becomes fully turbulent. It should be noted that there is no turbulent reattachment downstream of the transition region (observed from the continuously negative axial velocity near the wall in Fig. 7), as a result of the high adverse pressure gradient. The separated flow develops along the six measurement windows. In windows D through F, only reverse flow can be observed. The vorticity for 2-D flow is $\omega = \partial v / \partial x - \partial u / \partial y$. If taking only axial velocity into account, positive vorticity corresponds to

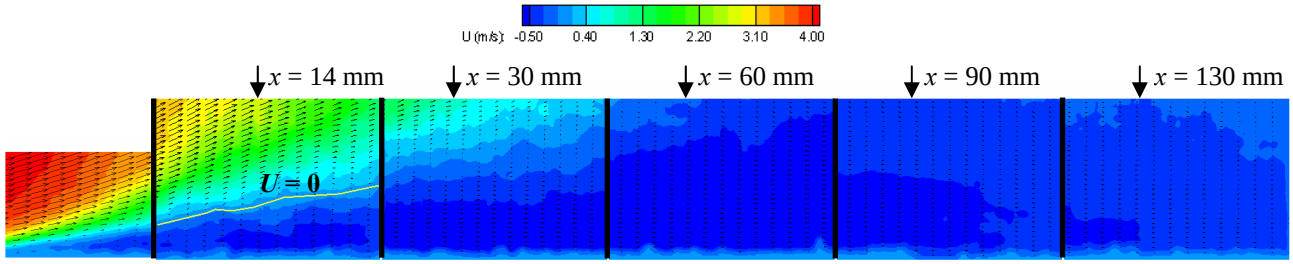

Figure 7: Velocity vectors and contours of axial velocity without actuation: (a)-(f) correspond to windows A-F in Fig. 6

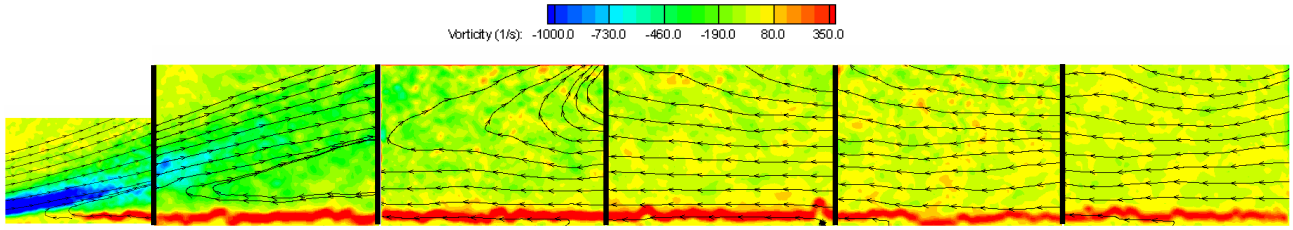

Figure 8: Streamlines and contours of vorticity without actuation: (a)-(f) correspond to windows A-F in Fig. 6

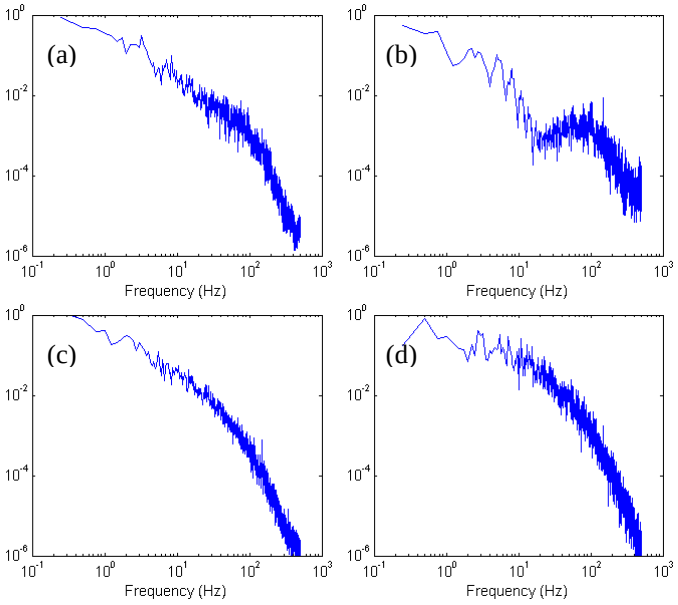

Figure 9: Power spectra of velocity fluctuation from hot-wire measurement without actuation at four diffuser locations in Fig. 6: (a), (c) and (d) inside the separated boundary layer; (b) at the boundary layer edge

$\partial u / \partial y < 0$ (increased amplitude of negative axial velocity with increased distance from the wall), while negative vorticity corresponds to $\partial u / \partial y > 0$ (increased amplitude of positive axial velocity with increased distance from the wall). In other words, the positive vorticity near the wall (in all windows of Fig. 8) corresponds to the reverse flow inside the separated boundary layer.

Fig. 9 shows power spectra of velocity fluctuations from hot-wire measurement without plasma actuation at four diffuser locations in Fig. 6, with two in the actuation plane (x = 0 mm) and two in the turbulent separation region (x = 90 mm). Please note that only the results in Fig. 9 are from hot-wire measurements, while other results presented later are from PIV measurement. Generally, there are various frequency peaks at each location. This indicates that large-scale vortices are shed from the separation bubble at those frequencies [23]. The corresponding lowest frequency is around 3 Hz, while the highest frequency is around 80 Hz (in Fig. 9(b)). Other frequencies include 5 Hz, 7.5 Hz and 15 Hz. The dimensionless frequencies $F^+ = fL_{se} / U_\infty$ corresponding to these frequencies are 0.18, 0.31, 0.46, 0.92 and 4.9, respectively (using the separation length L_{se} = 0.3 m and the area-averaged velocity at the diffuser throat plane U_∞ = 4.9 m/s). The frequency of 80 Hz (F^+ = 4.9) corresponds to the Kelvin-Helmholtz instability of the separated shear layer. The frequency of 3 Hz (F^+ = 0.18) appears to be related to an integral feature of a fully turbulent separation [23]. The optimal frequency for boundary layer separation control is $F^+ \sim O(1)$, based on the work by Herbst and Henningson [24] and Cierpka et al. [25]. In the present experiment, 15 Hz (F^+ = 0.92) is assumed to be the most effective frequency for separation control. This frequency and two other frequencies, namely 5 Hz (F^+ = 0.31) and 25 Hz (F^+ = 1.53), are chosen to demonstrate the effect of the actuation frequency.

Figs. 10 and 12 show the time-averaged velocity vectors and contours of axial velocity for cases with continuous actuation and pulsed actuation at 15 Hz, which corresponds to the most effective actuation in pulsed mode and will be discussed later. The streamlines and contours of the spanwise vorticity for the two cases above are shown in Figs. 11 and 13, respectively. Note that these figures represent time-averaged

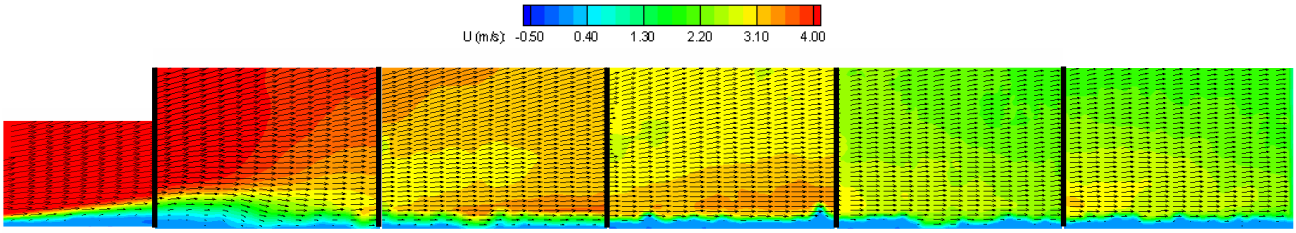

(a) (b) (c) (d) (e) (f)

Figure 10: Velocity vectors and contours of axial velocity with continuous actuation: (a)-(f) correspond to windows A-F in Fig. 6

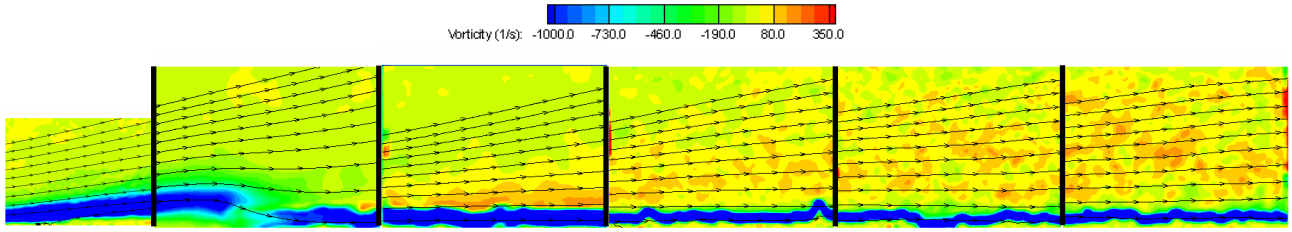

(a) (b) (c) (d) (e) (f)

Figure 11: Streamlines and contours of vorticity with continuous actuation: (a)-(f) correspond to windows A-F in Fig. 6

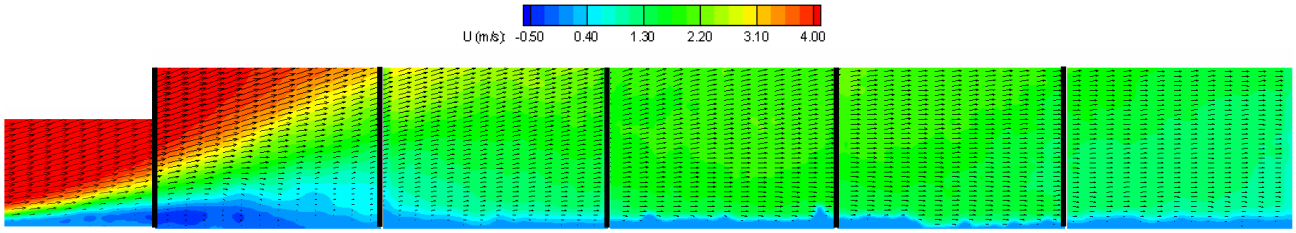

(a) (b) (c) (d) (e) (f)

Figure 12: Velocity vectors and contours of axial velocity with pulsed actuation: (a)-(f) correspond to windows A-F in Fig. 6

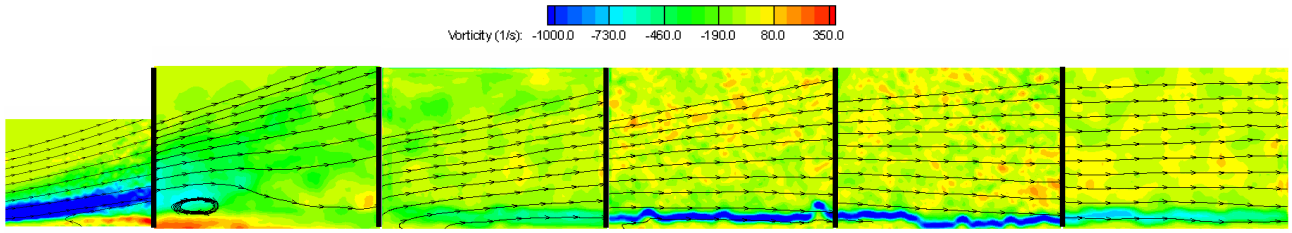

(a) (b) (c) (d) (e) (f)

Figure 13: Streamlines and contours of vorticity with pulsed actuation: (a)-(f) correspond to windows A-F in Fig. 6

flow fields.

Fig. 14 shows the measured axial velocity profiles from the PIV measurements for different cases, at five locations, namely 14 mm, 30 mm, 60 mm, 90 mm and 130 mm (diffuser exit) downstream of the actuator.

With plasma actuation, both continuous and pulsed, the turbulent separation is completely suppressed, as shown in Figs. 10, 12 and 14. The negative vorticity (in windows C through F of Figs. 11 and 13) corresponds to the streamwise flow affected by plasma actuation. However, as observed in windows A and B of Figs. 10 and 12, a small laminar separation bubble still exists. The separated shear layer can be clearly observed in windows A and B of Figs. 11 and 13. However, the separated shear layer is thinner than in the uncontrolled flow (see Fig. 7). The separated shear layer then reattaches near the actuation location in window B.

In a turbulent boundary layer with separation, large-scale structures supply the turbulence energy to the near-wall separated flow. This energy, however, is not sufficient to prevent boundary layer separation. Continuous actuation involves direct input of momentum or energy into the flow to prevent boundary layer separation. In contrast, pulsed actuation works by enhancing the mixing of high-momentum outer flow and low-momentum near-wall flow, or, by amplifying these

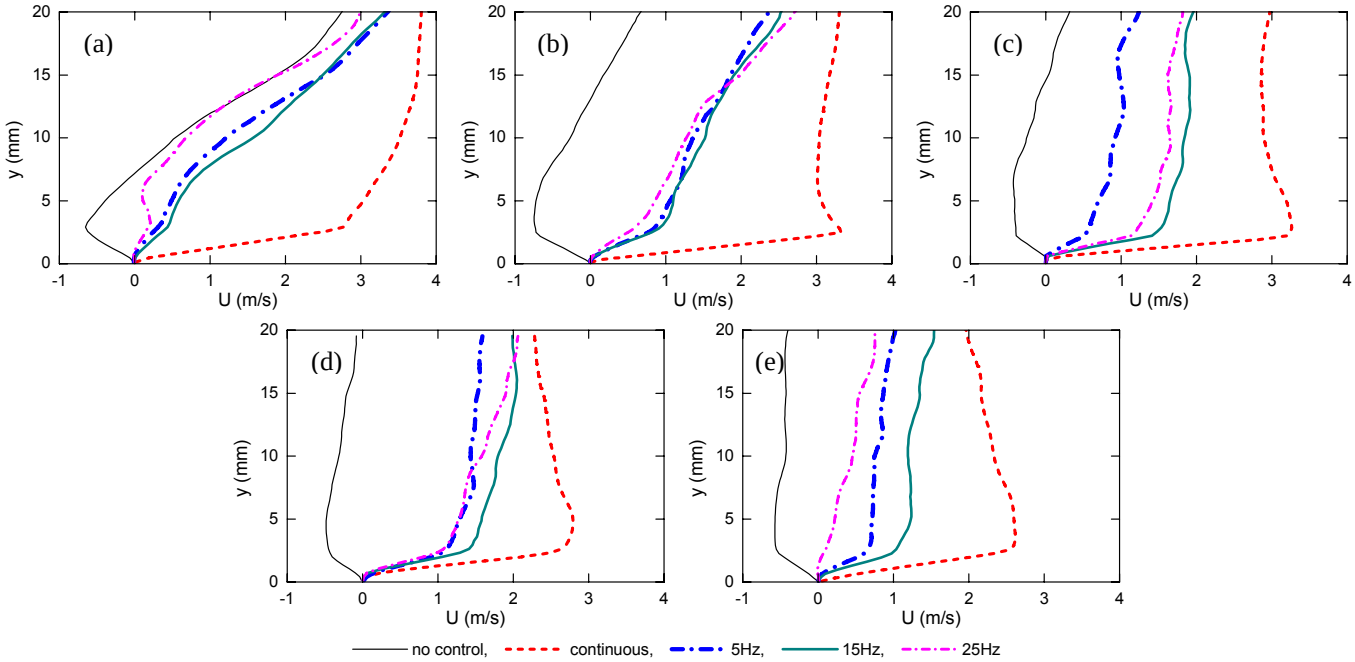

Figure 14: Axial velocity profiles at five locations downstream of actuation location: (a) 14 mm, (b) 30 mm, (c) 60 mm, (d) 90 mm, (e) 130 mm (diffuser exit)

large-scale structures within the boundary layer [26].

For the pulsed mode, the actuation frequency of 15 Hz is found to most effectively suppress the turbulent separation, as seen from the larger axial velocity at the chosen locations in Fig. 14. It should be noted that higher separation control effectiveness (reduced separation) corresponds to higher axial velocity at the diffuser throat. This is because the reduced separation can allow larger pressure recovery and lower static pressure at the test section inlet, and by extension higher mass flow rate for the same inlet total pressure and exit static pressure. The "bursting" frequency f of the most energetic eddies near the wall is correlated by $U / f\delta = 10$, where U is the mean velocity outside the boundary layer and δ is the boundary layer thickness [27]. In the present work, 15 Hz corresponds to this bursting frequency with $U = 3$ m/s and $\delta = 0.02$ m at $x = 0$ mm for the no-control case.

Concerning the variation of axial velocity versus axial distance in Fig. 14, the value with 15 Hz is always larger than that with 5 Hz and 25 Hz. In addition, the axial velocity with 5 Hz, compared to 25 Hz, is smaller in the near-actuation region (see Fig. 14(c)) while larger in the near-diffuser-exit region (see Fig. 14(e)). It should be noted that the present comparison is only for the axial range of x > 30 mm, excluding the actuator-related effects, based on two considerations: 1) a recirculation zone exists in the vicinity of the upper electrode (-12.7 mm < x < 0 mm)[28], and 2) the process of momentum addition from plasma actuator ranges a distance over the lower electrode (maximum distance is same as the lower electrode width of 25.4 mm). As discussed above, the mechanism of separation control by pulsed actuation involves the mixing enhancement of high-momentum outer flow with the low-momentum near-wall flow. The mixing enhancement can be achieved through a series of vortices generated by pulsed plasma actuation. Increased actuation frequency results in a mean flow with a more focused wall jet and higher velocity overshoots closer to the surface [13]. The pulsed actuation with 25 Hz thus has more effect on near-wall flow than 5 Hz. On the other hand, the pulsed actuation with 5 Hz has more effect on the boundary layer edge and generates larger vortices with associated stronger flow mixing. Therefore, the effect of pulsed actuation with 25 Hz is more immediate while less downstream. However, pulsed actuation with 5 Hz has a larger time/length scale and its effect on the flow can extend further downstream.

The continuous actuation is more effective on the suppression of this turbulent separation. The free-stream velocity in all windows of Figs. 10 and 12 is larger for the continuous actuation than the pulsed actuation with 15 Hz, indicating higher mass flow. The axial velocity at the diffuser exit for continuous actuation is twice as high as that of the pulsed actuation with 15 Hz (see Fig. 14(e)). However, it must be noted that pulsed actuation has a 30% duty cycle and thus consumes only 30% of the power of continuous actuation.

3.2 Flow Fluctuation

In contrast to the time-averaged flow fields with boundary layer separation, instantaneous flow fields are significantly different (e.g., time-varying velocity, combination of various turbulent structures, variation of instantaneous separation

point), especially for the cases without and with pulsed actuation.

To describe the different states of turbulent flow detachment near the wall, a set of definitions based on the forward-flow-fraction γ_{pu} includes ID, ITD, TD and D (see Fig. 1). The points TD and D generally are at the same axial location. The TD point can be evaluated as a position where γ_{pu} near the wall reaches the value 0.5, while the D point corresponds to a position with zero mean axial velocity (zero mean axial shear stress) near the wall. Fig. 15 shows the fraction of positive axial velocity in window B for different cases without actuation, with continuous actuation and with pulsed actuation at 15 Hz, respectively. Since the boundary layer separates just downstream of the throat and no attachment is observed in Fig. 7(a), direct comparison of TD and D is not available. However, the curve with zero mean axial velocity in Fig. 7(b) and the curve with γ_{pu} = 0.5 in Fig. 15(a) match well. With the separation suppressed by both continuous and pulsed actuations, the region with low γ_{pu} is also suppressed. The curve with γ_{pu} = 0.5 in Figs. 15(b) and (c) also match well with the curve with zero mean axial velocity in Figs. 10(b) and 12(b), respectively.

In a turbulent boundary layer with separation, large-scale structures supply the turbulence energy to the near-wall separated flow. Thus turbulent kinetic energy (TKE) in the flow is an important parameter for both no-control and actuation cases as an indicator of control effectiveness. Since the instantaneous values of the TKE can vary substantially, the mean TKE values are preferred as more representative of the overall flow. The mean TKE in 2-D flows is given by

$$ke = \frac{1}{2}\frac{\overline{uu}+\overline{vv}}{U_{throat}^2} \qquad (1)$$

where u and v denote the primary (axial) and secondary (normal) components of the fluctuating velocity, respectively.

Fig. 16 shows the TKE in window B for different cases. For the no-control case, the maximum TKE is located above the curve of zero mean axial velocity (Fig. 7(b)). In other words, the maximum fluctuations are in the middle of the separated boundary layer, which is different from the zero-pressure-gradient case (the maximum is near the wall)[2]. With continuous actuation, the TKE is substantially reduced in most of the region, implying that the controlled flow is much steadier. However, with pulsed actuation, the maximum TKE is increased while the region of high TKE is decreased. This is because the separation is suppressed by the mixing enhancement of high-momentum outer flow and low-momentum inner flow. It should be noted that the maximum TKE for the case with pulsed actuation is also located in the middle of the boundary layer.

The contribution of the TKE in axial and normal directions can be decomposed by computing the normal turbulent Reynolds stresses $\overline{uu}/U_{throat}^2$, $\overline{vv}/U_{throat}^2$ and the shear

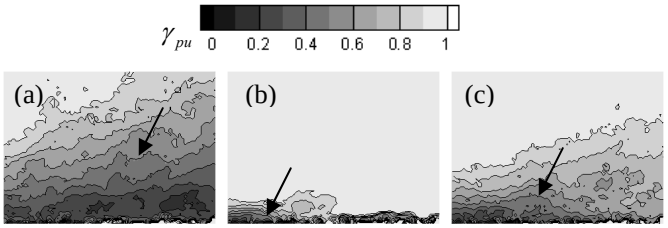

Figure 15: Fraction of positive axial velocity in window B (arrows indicate γ_{pu} = 0.5) with (a) no actuation, (b) continuous actuation, (c) pulsed actuation at 15 Hz

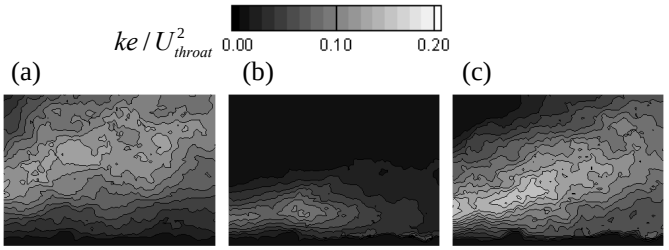

Figure 16: Turbulent kinetic energy in window B with (a) no actuation, (b) continuous actuation, (c) pulsed actuation at 15 Hz

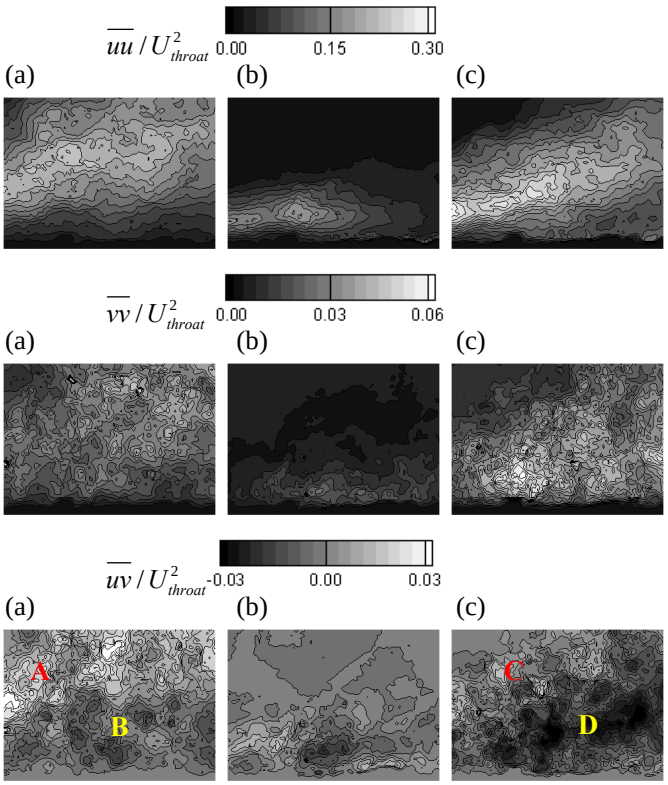

Figure 17: Turbulent Reynolds stresses in window B with (a) no actuation, (b) continuous actuation, (c) pulsed actuation at 15 Hz

turbulent Reynolds stress $\overline{uv}/U_{throat}^2$. The turbulent Reynolds stresses indicate the contribution of turbulent motion (fluctuation) to the mean momentum transfer, of which the shear Reynolds stress $\overline{uv}/U_{throat}^2$ plays a dominant role [29]. Fig. 17 shows the turbulent Reynolds stresses in window B for different cases. It can be observed that the $\overline{uu}/U_{throat}^2$ component is the main source of the TKE for all cases. As for $\overline{uv}/U_{throat}^2$, the maximum positive values for cases without and with pulsed actuation (A and C in Fig. 17) are located near the boundary layer edge, while the maximum negative values (B and D in Fig. 17) are located in the middle of the boundary layer. The distribution of negative $\overline{uv}/U_{throat}^2$ is consistent with that for turbulent boundary layer separation on flat surfaces [2], which indicates the momentum transfer by turbulent fluctuation from the high-momentum outer flow to low-momentum near-wall flow. In contrast, the positive $\overline{uv}/U_{throat}^2$ near the boundary layer edge indicates the entrainment process from the boundary layer to the outer-flow, induced by the high diffusion rate especially just downstream of the diffuser throat. In addition, the maximum negative $\overline{uv}/U_{throat}^2$ is larger for pulsed actuation than for no-control case (D versus B in Fig. 17), corresponding to the increased momentum transfer by flow fluctuation resulting from pulsed actuation.

3.3 POD Analysis

Topos and Chronos

Fig. 18 shows 1-D topos (1-D decomposition on vertical lines) of the axial velocity in the plane at x = 14 mm with continuous actuation, while Fig. 19 shows corresponding chronos. The topos demonstrates the increasing number of changes in sign with increasing mode number. Generally, the first mode of the POD is representative of the mean, as observed from the almost constant non-zero chronos for the first mode in Fig. 19 and compared with mean axial velocity in Fig. 14. Other modes represent the fluctuation in the flow with different length/time scales, with the continually altered sign of corresponding chronos. The second mode is thus representative of the fluctuation with large scale (large flow structures).

It should be noted that the sign of topos/chronos is not important but their product has a physical meaning. For example, the negative value of mode 1 in Fig. 18 associated with the negative value of mode 1 in Fig. 19 represents the positive axial velocity, resulting from the separation suppression by the plasma actuation.

Figs. 20 and 21 show the development of the second mode of the 1-D topos versus axial distance for cases with no actuation and continuous actuation, respectively. Note that the topos magnitudes in these two figures are not necessarily the same. The location in the normal direction with peak value of the topos is lower for the case with continuous actuation than that for the no-control case. This is because plasma actuation suppresses the turbulent boundary layer separation and at the same time reduces the fluctuation within the boundary layer. The fluctuation length scale in the normal direction (wall-

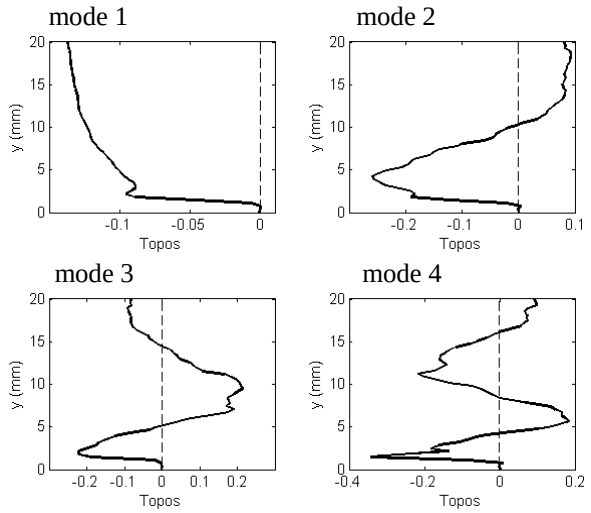

Figure 18: Topos of axial velocity at the location of *x* = 14 mm with continuous actuation

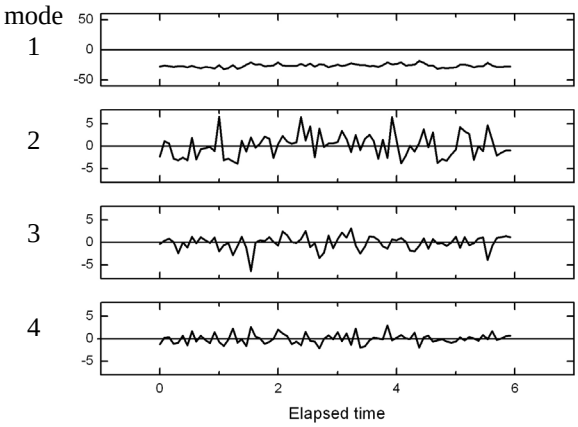

Figure 19: Chronos of axial velocity at the location of *x* = 14 mm with continuous actuation

distance of the zero-crossing of the second modes) increases versus axial distance, as observed from Fig. 20(a-c), Fig. 21(a-c) and Fig. 21(d-g), respectively. This is a reflection of the downstream development of the normal spreading of the shear layer [30]. For the case with continuous actuation, the flow control reshapes the boundary layer, with the associated new development of fluctuations (length scale in the normal direction) in Fig. 21(d-g). This trend of the length scale is consistent with that of the boundary layer thickness in the mean flow (see Fig. 10), which can endure more adverse pressure gradient without separation.

Energy Distribution

Fig. 22 shows the eigenvalues (energy distribution) for different cases at the location x = 30 mm. From this figure, it is observed that the POD converges rapidly, with the energy rapidly decreases with the mode number. The case with continuous actuation converges fastest because the main energy

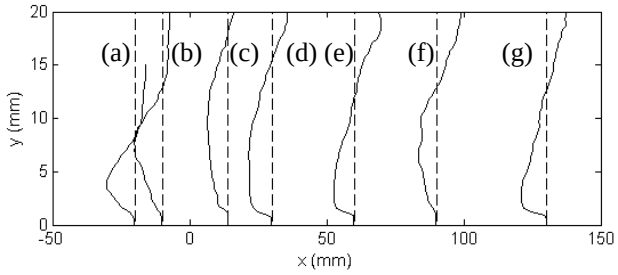

Figure 20: Development of second mode of topos without actuation

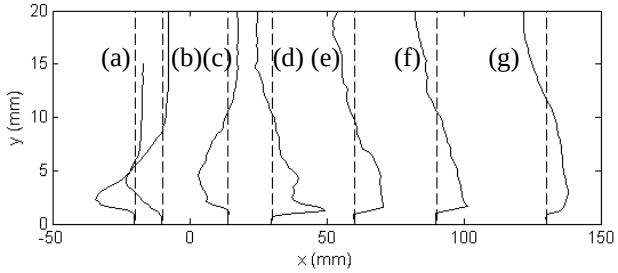

Figure 21: Development of second mode of topos with continuous actuation

is included in the mean, while the no-control case converges slowest because quite a lot of energy is included in the fluctuation associated with the separated flow. This is consistent with Simpson's argument [2] that the velocity fluctuations in the reverse flow region are greater than or at least comparable to the mean reverse velocities.

Entropy Development

The cumulated entropy (see Eqn. (6)) increases with mode number, because the addition of higher mode increases the disorder of the whole system. For the cases in this paper, the cumulated entropy almost reaches the maximum at the mode number of 20. The maximum cumulated entropy is thus a global entropy (abbreviated as entropy in the following presentation). Fig. 23 shows the development of entropy versus axial distance for different cases. With no actuation, the entropy reaches a maximum in the middle part ($x \approx 30$ mm). This is because the energy upstream of this location is mainly included in the positive mean flow while downstream it is in the reverse mean flow. With both continuous and pulsed actuation, the entropy is reduced at each location, implying that the flow is more stable and more energy is included in the mean flow. Moreover, it is observed that a local minimum entropy exists for all cases between actuation location and diffuser exit. In terms of the local minimum entropy, the continuous actuation has the most upstream location, followed by pulsed actuation at 15 Hz and 25 Hz, and 5 Hz with the most downstream location. This can be explained by the fact that the further upstream the location with local minimum entropy, the earlier the effect of actuation on the flow is activated. This trend is consistent with

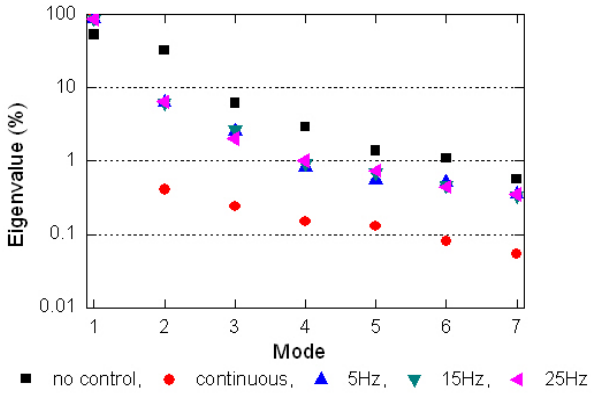

Figure 22: Energy distribution at the location of x = 30 mm

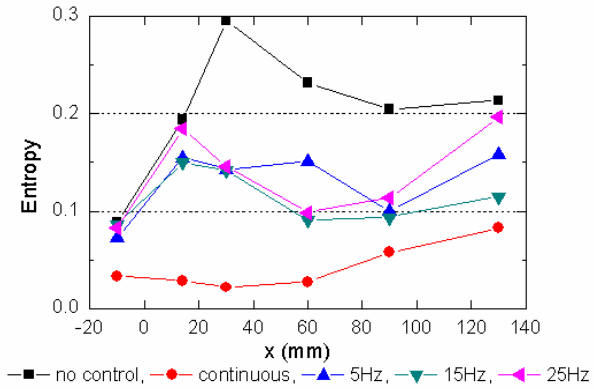

Figure 23: Development of entropy

the development of mean velocity in Fig. 14. In addition, near the diffuser exit, the entropy increases again for all cases, since the plasma actuation is far from this location, and its effect is significantly reduced.

Since the entropy is a normalized quantity, it can be used to compare the disorder levels of different signals. In other words, it can be used in this paper to quantify the effects of different plasma actuation regimes on boundary layer separation control. The smaller the entropy, the more effective the control. As shown in Fig. 23, the continuous actuation is most effective, followed by the pulsed actuation at 15 Hz.

Spectra

The spectra of axial velocity fluctuation based on PIV measurement can also show some features of the flow with pulsed actuation, even though the sampling frequency f_s is not high enough. Fig. 24 show the spectra of axial velocity fluctuation in the plane of x = 30 mm, without actuation and with pulsed actuation, respectively. The spectrum for the case without actuation is more complex than that with pulsed actuation, indicating that the flow with pulsed actuation is more organized. The near-wall flow for each case has smaller fluctuation, as observed from the lower spectrum power near the wall. In addition, the spectra for each case reveal the similar distributions for different frequencies along the normal location

in the same plane, and thus these spectra at the same axial location can be averaged to obtain a smooth one.

Fig. 25 shows the average spectra of axial velocity fluctuation for different cases in the plane of x = 30 mm and 90 mm. Because of the low sampling frequency f_s and thus aliasing effect, the observed frequencies f_{ob} with peak values are not the realistic ones f_{real} within the flow. The corresponding relation is [31]

$$f_{real} = f_{ob} + 2Nf_N \quad or \quad = -f_{ob} + (2N+1)f_N \qquad (N = 0,1,2\cdots) \qquad (2)$$

where $f_N = f_s/2$ is the Nyquist frequency (7 Hz for most cases, except 6.5 Hz for the no-control case). For example, f_{ob} = 1 Hz could correspond to f_{real} = 15 Hz with N = 1, f_N = 7 Hz. For the no-control case in Fig. 25, various peaks can be observed, which is qualitatively similar to the spectra from hotwire measurement (Fig. 9). This also indicates that large-scale vortices are shedding from the separation bubble over those frequencies [23]. For the cases with pulsed actuation, the shedding of large-scale vortices in the flow at x = 30 mm is locked on the actuation frequencies of 5 Hz, 15 Hz and 25 Hz (as observed from the sharp peaks at f_{ob} = 5 Hz, 1 Hz and 3 Hz), respectively. This is consistent with the finding of Hwang et al. [32]. For the 5 Hz case, another observed frequency 4 Hz may correspond to a superharmonic frequency of 10 Hz. However, the situation at x = 90 mm is different, with more peaks observed. This is because this location is far from the actuation source and the effect of actuation is less significant.

4. CONCLUSION

The present paper studies the effects of DBD plasma actuators experimentally on suppression of a 2-D turbulent boundary layer separation in a diffuser with high adverse pressure gradient. Both continuous and pulsed actuations are applied and shown to effectively suppress the turbulent boundary layer separation. For the pulsed actuation, the actuation frequency of 15 Hz, corresponding to the dimensionless frequency of $F^+ \sim O(1)$, is found to the most effectively suppress the turbulent separation. The variations of turbulent kinetic energy and Reynolds shear stress demonstrate the increased momentum transfer by fluctuations in the flow with pulsed actuation. To better analyze the results from PIV measurements, the POD method was applied to extract the spatial modes and their temporal counterparts. The effect of continuous actuation can be demonstrated by the variation of the second spatial mode (corresponding to large fluctuation in the flow). Moreover, the entropy, indicating the energy distribution of various modes, is proposed to quantify the effects of different plasma actuation regimes on boundary layer separation control. In addition, from spectral analysis the flow with pulsed actuation is observed to be locked on the actuation

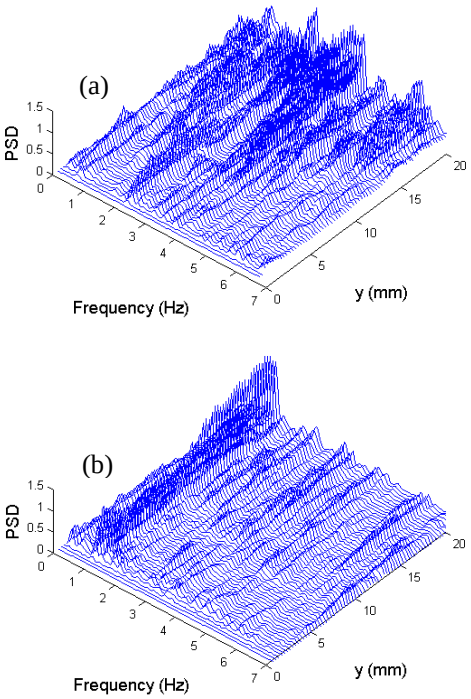

Figure 24: Spectra of axial velocity fluctuation at the location of x = 30 mm with (a) no actuation, (b) pulsed actuation

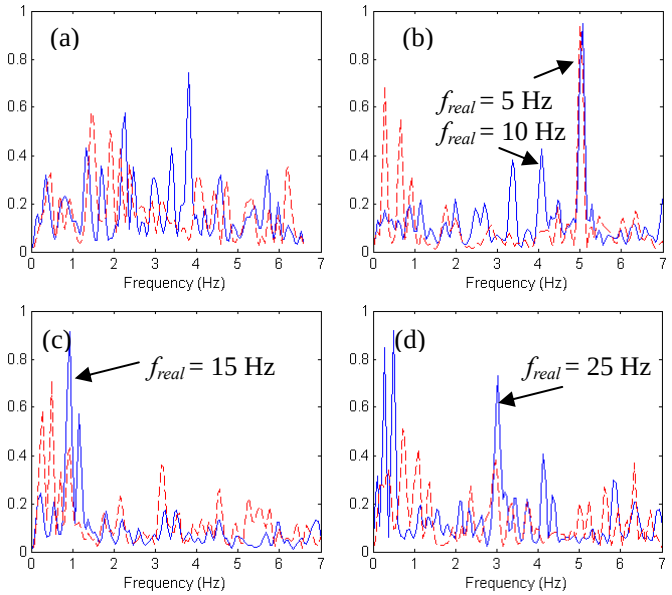

Figure 25: Averaged spectra of axial velocity fluctuation at the locations of x = 30 mm (solid blue line) and 90 mm (dashed red line) for the cases with (a) no actuation, (b) pulsed actuation at 5 Hz, (c) pulsed actuation at 15 Hz, (d) pulsed actuation at 25 Hz

frequencies near the actuation location, while the result is not obvious far from the actuation location.

ACKNOWLEDGMENTS

The authors are pleased to acknowledge the support from the National Research Council Canada (NRC) and the assistance of Mr. P. Versailles, Mr. S. Ueno and Mr. K. Huynh at École Polytechnique de Montréal with the experimental setup.

REFERENCES

[1] Simpson, R. L., 1981, "A Review of Some Phenomena in Turbulent Flow Separation," Journal of Fluids Engineering, **103**(4), pp. 520-533.

[2] Simpson, R. L., 1996, "Aspects of Turbulent Boundary-Layer Separation," Progress in Aerospace Sciences, **32**(5), pp. 457-521.

[3] Sullerey, R. K., Mishra, S., and Pradeep, A. M., 2002, "Application of Boundary Layer Fences and Vortex Generators in Improving Performance of S-Duct Diffusers," Journal of Fluids Engineering, Transactions of the ASME, **124**(1), pp. 136-142.

[4] Pradeep, A. M., and Sullerey, R. K., 2006, "Active Flow Control in Circular and Transitioning S-Duct Diffusers," Journal of Fluids Engineering, Transactions of the ASME, **128**(6), pp. 1192-1203.

[5] Mathis, R., Duke, D., Kitsios, V., and Soria, J., 2008, "Use of Zero-Net-Mass-Flow for Separation Control in Diffusing S-Duct," Experimental Thermal and Fluid Science, **33**(1), pp. 169-172.

[6] Shin, J., Narayanaswamy, V., Raja, L. L., and Clemens, N. T., 2007, "Characterization of a Direct-Current Glow Discharge Plasma Actuator in Low-Pressure Supersonic Flow," AIAA Journal, **45**(7), pp. 1596-1605.

[7] Enloe, C. L., Mclaughlin, T. E., Vandyken, R. D., Kachner, K. D., Jumper, E. J., and Corke, T. C., 2004, "Mechanisms and Responses of a Single Dielectric Barrier Plasma Actuator: Plasma Morphology," AIAA Journal, **42**(3), pp. 589-594.

[8] Forte, M., Jolibois, J., Pons, J., Moreau, E., Touchard, G., and Cazalens, M., 2007, "Optimization of a Dielectric Barrier Discharge Actuator by Stationary and Non-Stationary Measurements of the Induced Flow Velocity: Application to Airflow Control," Experiments in Fluids, **43**(6), pp. 917-928.

[9] Roth, J. R., and Dai, X., 2006, "Optimization of the Aerodynamic Plasma Actuator as an Electrohydrodynamic (EHD) Electrical Device," AIAA Paper 2006-1203.

[10] Patel, M. P., Ng, T. T., Vasudevan, S., Corke, T. C., Post, M. L., Mclaughlin, T. E., and Suchome, C. F., 2008, "Scaling Effects of an Aerodynamic Plasma Actuator," Journal of Aircraft, **45**(1), pp. 223-236.

[11] Orlov, D. M., Apker, T., He, C., Othman, H., and Corke, T. C., 2007, "Modeling and Experiment of Leading Edge Separation Control Using SDBD Plasma Actuators," AIAA Paper 2007-0877.

[12] Rizzetta, D. P., and Visbal, M. R., 2008, "Plasma-Based Flow-Control Strategies for Transitional Highly Loaded Low-Pressure Turbines," Journal of Fluids Engineering, Transactions of the ASME, **130**(4), pp. 0411041-04110412.

[13] Visbal, M. R., and Gaitonde, D. V., 2006, "Control of Vortical Flows Using Simulated Plasma Actuators," AIAA Paper 2006-505.

[14] Hultgren, L. S., and Ashpis, D. E., 2003, "Demonstration of Separation Delay with Glow-Discharge Plasma Actuators," AIAA Paper 2003-1025.

[15] Boxx, I. G., Woods, N. M., Newcamp, J. M., Franke, M. E., and Rivir, R. B., 2006, "A PIV Study of a Plasma Discharge Flow-Control Actuator on a Flat Plate in an Aggressive Pressure Induced Separation," ASME Paper GT2006-91044.

[16] Schlichting, H., 1979, Boundary-Layer Theory, McGraw-Hill, New York, Origin of Turbulence.

[17] Visbal, M. R., Gaitonde, D. V., and Roy, S., 2006, "Control of Transitional and Turbulent Flows Using Plasma-Based Actuators," AIAA Paper 2006-3230.

[18] He, C., Corke, T. C., and Patel, M. P., 2007, "Numerical and Experimental Analysis of Plasma Flow Control over a Hump Model," AIAA Paper 2007-935.

[19] Hemon, P., and Santi, F., 2003, "Applications of Biorthogonal Decompositions in Fluid-Structure Interactions," Journal of Fluids and Structures, **17**(8), pp. 1123-1143.

[20] Aubry, N., Guyonnet, R., and Lima, R., 1991, "Spatiotemporal Analysis of Complex Signals: Theory and Applications," Journal of Statistical Physics, **64**(3-4), pp. 683-739.

[21] Hoarau, Y., Braza, M., Ventikos, Y., and Faghani, D., 2006, "First Stages of the Transition to Turbulence and Control in the Incompressible Detached Flow around a Naca0012 Wing," International Journal of Heat and Fluid Flow, **27**(5), pp. 878-886.

[22] Mathis, R., Lebedev, A., Collin, E., Delville, J., and Bonnet, J. P., 2009, "Experimental Study of Transient Forced Turbulent Separation and Reattachment on a Bevelled Trailing Edge," Experiments in Fluids, **46**(1), pp. 131-146.

[23] Cherry, N. J., Hillier, R., and Latour, M. E. M. P., 1984, "Unsteady Measurements in a Separated and Reattaching Flow," Journal of Fluid Mechanics, **144**, pp. 13-46.

[24] Herbst, A. H., and Henningson, D. S., 2006, "The Influence of Periodic Excitation on a Turbulent Separation Bubble," Flow, Turbulence and Combustion, **76**(1), pp. 1-21.

[25] Cierpka, C., Weier, T., and Gerbeth, G., 2007, Active Flow Control, Springer, Berlin, Electromagnetic Control of Separated Flows Using Periodic Excitation with Different Wave Forms.

[26] Gad-El-Hak, M., 2000, *Flow Control : Passive, Active, and Reactive Flow Management*, Cambridge University Press, Cambridge, U.K. ; New York.
[27] Simpson, R. L., Strickland, J. H., and Barr, P. W., 1977, "Features of a Separating Turbulent Boundary Layer in the Vicinity of Separation," Journal of Fluid Mechanics, **79**, pp. 553-594.
[28] Kriegseis, J., Dehler, T., Pawlik, M., and Tropea, C., 2009, "Pattern-Identification Study of the Flow in Proximity of a Plasma Actuator," AIAA Paper 2009-1001.
[29] Tennekes, H., and Lumley, J. L., 1972, *A First Course in Turbulence*, The MIT Press, Cambridge and London.
[30] Manhart, M., and Wengle, H., 1993, "A Spatiotemporal Decomposition of a Fully Inhomogeneous Turbulent Flow Field," Theoretical and Computational Fluid Dynamics, **5**(4), pp. 223-242.
[31] Aliasing, April 29 2010, http://en.wikipedia.org/wiki/Aliasing#cite_ref-mitchell_0-0
[32] Hwang, K. S., Sung, H. J., and Hyun, J. M., 2001, "An Experimental Study of Large-Scale Vortices over a Blunt-Faced Flat Plate in Pulsating Flow," Experiments in Fluids, **30**(2), pp. 202-213.

APPENDIX
Proper Orthogonal Decomposition (POD)

In the POD, a turbulent space-time velocity field $\tilde{u}_i(\vec{x},t)$ (i = 1, 2, 3) can be split as [19]

$$\tilde{u}_i(\vec{x},t)=\sum_{k=1}^{\infty}\psi_k(t)\varphi_{ik}(\vec{x}) \tag{3}$$

where $\varphi_{ik}(\vec{x})$ is the spatial mode (called *topos*) of order k and $\psi_k(t)$ is the corresponding temporal mode (called *chronos*). Each combination of $\psi_k\varphi_{ik}$ represents a basic state embedded in the random turbulent flow field.

To solve Eqn. (3), the singular value decomposition of matrix A is applied

$$A=U\sum V^T=QV^T \tag{4}$$

where U and V are orthogonal and $\sum$ is a diagonal matrix whose coefficients α_k are the singular values of A. Thus Eqn. (3) is solved, with Q and V corresponding to ψ and φ, respectively.

The eigenvalues λ_k ($\lambda_k=\alpha_k^2$) is representative of the energy associated with the mode k. Thus the global energy of the signal is equal to the sum of the eigenvalues

$$\sum_{k=1}^{\infty}\lambda_k=\sum_{k=1}^{\infty}\alpha_k^2 \tag{5}$$

The global entropy of the signal characterizing its degree of disorder is defined as [20]

$$H=-\lim_{M\to\infty}\frac{1}{\log M}\sum_{k=1}^{M}\lambda_{rk}\log\lambda_{rk} \tag{6}$$

with

$$\lambda_{rk}=\lambda_k/\sum_{k=1}^{\infty}\lambda_k \tag{7}$$

where M is the total mode number (M = 73 in the present paper).

